Chemical Engineering & Technology

Chemical & Engineering Technology

RESEARCH ARTICLE OPEN ACCESS

DEM–CFD Investigation of Packing Structure Effects on the Thermal Decomposition of Limestone

Rezvan Abdi | Bo Jaeger | Torben Bergold | Enric Illana | Martin Schiemann | Viktor Scherer

Institute of Energy Plant Technology, Ruhr-University Bochum, Bochum, Germany

Correspondence: Rezvan Abdi (Abdi@leat.ruhr-uni-bochum.de)

Received: 27 October 2025 | **Revised:** 8 May 2026 | **Accepted:** 14 May 2026

Keywords: average volume method (AVM) | calcination | discrete element method (DEM) | DOM radiation | lime production

ABSTRACT

A radiation model based on the discrete ordinates method (DOM) is integrated into a discrete element method (DEM)–computational fluid dynamics (CFD) framework to simulate limestone calcination in a moving particle bed with gas flow. Local porosity of the particle bed is incorporated into the model to compute the effective radiative heat transfer for different packing densities. The endothermic calcination reaction converts $CaCO_3$ into CaO. The article evaluates radiation penetration, temperature distributions, calcination degree, and CO_2 mass fraction in the system. Convective, radiative, and particle–particle conductive heat transfer are considered for dilute, moderate, and dense packing densities. Results show that packing density strongly influences both radiation and calcination. The study shows that the calcination degree decreases with increasing packing density. The simulation results yield average calcination degrees of 98%, 80%, and 60% for particles at outlet in the dilute, moderate, and dense configurations, respectively.

1 | Introduction

Quicklime (CaO) plays a crucial role in various industrial applications, including steel manufacturing, wastewater treatment, and flue gas desulfurization. Its production is based on the thermal decomposition of limestone ($CaCO_3$) through calcination, which is commonly carried out in shaft kilns. Calcination is a thermally driven endothermic reaction that requires 178 kJ mol^{-1} to decompose calcium carbonate into calcium oxide and carbon dioxide ($CaCO_3(s) \rightarrow CaO(s) + CO_2(g)$).

To achieve a realistic description of the calcination phenomena, researchers have investigated the application of the discrete element method (DEM). This approach solves the motion and interactions among individual particles according to Newton's laws of motion [1]. DEM is a highly effective tool for studying the dynamics of particle-based systems due to its ability to easily access information at the individual particle level [2]. When coupled with computational fluid dynamics (CFD), a comprehensive analysis of thermochemical processes becomes feasible by modeling particle dynamics, particle reaction, and gas-phase interactions. However, due to the computational challenges posed by the large number of particles in industrial-scale kilns, DEM-based shaft kiln simulations remain relatively scarce. Examples for DEM–CFD simulations used to investigate different shaft kiln configurations can be found in [3–5].

Intra-particle heat and mass transfer adds another layer of complexity to kiln modeling. The particles in lime production are thermally thick, and hence, gradients of temperature and species must be resolved in the interior of the particle. In previous work [6], the particles are modeled as spheres, and the calcination pro-

Abbreviations: AVM, average volume method; CFD, computational fluid dynamics; CV, control volume; DOM, discrete ordinates method; DEM, discrete element method; RTE, radiative transfer equation.

cess is simulated using a shrinking core model, where the outer layer of the particle reacts first, gradually transitioning to the core as the reaction progresses. In another approach [3–5, 7], thermally thick particles are modeled by discretizing the spherical particles into concentric shells. Each shell is assumed to have a uniform temperature, and heat conduction and mass transfer are solved radially through the particle. The same approach is used in this study. Recently, Mieg et al. [8] developed and validated reduced-order models to efficiently simulate calcination in thermally thick particles. The model significantly reduces computation time while maintaining accuracy.

A notable gap in current research is the absence of detailed 3D DEM–CFD studies for lime production that accurately incorporate radiation effects using the discrete ordinates method (DOM). In this study, the DOM approach is employed due to its ability to effectively capture the directional variability of radiation.

In DEM–CFD simulations involving large numbers of particles, the bulk can be efficiently represented within the Eulerian CFD framework using the average volume method (AVM). Instead of individually resolving the particles and the voids between them [9], this method represents particles through a porosity field and all relevant properties are volume-averaged. The transfer of mass, energy, and species is computed for each particle and then distributed across the CFD domain accordingly. As a result, the precise shape of individual particles is not resolved during the CFD simulation.

In this study, to enable efficient computation, AVM is utilized by deriving a time-resolved porosity distribution from DEM. This strategy allows for multiple particles to be contained within a single CFD control volume (CV), enabling the modeling of solid-fluid interactions at subgrid interfaces. The AVM model used here considers radiation shadowing between "particle layers" in adjacent fluid cells [10].

A major contribution of this study is the detailed investigation of heat transfer mechanisms—including convection, contact conduction, and radiation—within a moving packed particle system. By adjusting absorption and emission coefficients in the DOM for varying packing densities, the study ensures accurate distribution of radiative heat in fluid cells. The accuracy of this adjustment has been validated through comparison with both experimental and numerical data reported in our previous publication [10]. Additionally, for cases where only the overall effect of radiation shadowing is of interest, this approach may eliminate the necessity of particle-particle radiation modeling. This study is an extension of our previous work [10], in which calcination was not considered, and the results were obtained at much smaller particle residence times.

The proposed model has been integrated into an in-house DEM software, developed within the bulk-reaction research center [11], supported by funding from the German Research Foundation. The DEM software is coupled with OpenFOAM [12] to solve for the energy, species, and mass transport in the gas phase. Section 2 introduces the calcination and radiation modeling approach, followed by a comparative analysis of calcined and uncalcined cases in Section 3 and a summary of key findings in Section 4.

2 | Model Description

2.1 | Discrete Element Method

Each particle is represented as an isotropic, homogeneous porous material. The equations governing heat and mass transfer, as well as chemical reactions, are solved for each particle. The DEM framework is used to represent individual particle reactions, but particle motion and interactions are not explicitly solved; instead, particles follow prescribed trajectories with fixed velocities.

2.2 | Computational Fluid Dynamics

The CFD component ensures mass, momentum, and energy conservation in the fluid phase by solving the following transport equations:

$$\frac{\partial \phi \rho_f}{\partial t} + \nabla \cdot \left(\phi \rho_f \mathbf{u_f}\right) = S_{\text{gas}} \tag{1}$$

$$\frac{\partial \left(\phi \rho_f \vec{\mathbf{u}}_\mathbf{f}\right)}{\partial t} + \nabla \cdot \left(\phi \rho_f \mathbf{u_f} \mathbf{u_f}\right) = -\phi \nabla p + \phi \nabla \cdot \boldsymbol{\tau}_\mathbf{f} + \phi \rho_f \mathbf{g} + \mathbf{S_M} \tag{2}$$

$$\frac{\partial \left(\phi \rho_f h_f\right)}{\partial t} + \nabla \cdot \left(\phi \rho_f \mathbf{u_f} h_f\right) = \nabla \cdot \left(\phi\, k_f\, \nabla T\right) + S_E \tag{3}$$

The fluid phase is characterized by its velocity $\mathbf{u_f}$, density ρ_f, porosity ϕ, and specific enthalpy h_f. In these fluid equations, the local bed porosity ϕ (provided by the DEM model for each fluid cell) is used. S_{gas} is the mass (air and CO_2) exchanged with the solid phase. The momentum source terms include the pressure gradient ∇p, the stress tensor $\boldsymbol{\tau}_\mathbf{f}$ (assuming laminar flow), the gravitational acceleration $\mathbf{g}$ and the momentum exchanged with the particles $\mathbf{S_M}$. In this formulation, $\mathbf{S_M}$ is determined using the Ergun equation [13, 14]. In the energy equation, the fluid's thermal conductivity is represented by k_f, whereas the enthalpy exchange with the solid phase corresponds to S_E.

The transport equation for chemical species is expressed as

$$\frac{\partial \left(\phi \rho_f Y_{\text{CO}_2}\right)}{\partial t} + \nabla \cdot \left(\phi \rho_f \mathbf{u_f} Y_{\text{CO}_2}\right) = \nabla \cdot \left(\phi \rho_f D_{\text{CO}_2} \nabla Y_{\text{CO}_2}\right) + S_{\text{CO}_2} \tag{4}$$

The gas phase comprises the components H_2O, CO_2, N_2, and O_2. To simplify the modeling process, the species transport equation is solved only for the mass fraction Y_{CO2}, as it significantly influences the calcination rate of lime particles. Additionally, the source term S_{CO_2} and the term including the diffusion coefficient D_{CO_2} model the release and transport of CO_2 from the particles during the calcination reaction, respectively.

2.3 | Convective and Conductive Heat Transfer

The convective heat transferred, $\dot{Q}_{\text{conv}}$ (W), is given by:

$$\dot{Q}_{\text{conv}} = \alpha A_p \left(T_f - T_{p,\text{surf}}\right) \tag{5}$$

where T is the temperature, A_p represents the particle's surface area, and α denotes the convective heat transfer coefficient. Further details on the calculation of α can be found in [5].

The contact heat transfer among particles is influenced by two main mechanisms: heat conduction through particle contact points and the gas layer in the vicinity of the contact points. Details of the equations can be found in Hilse et al. [15].

2.4 | Radiation Model

Equation (6) provides a simplified form of the radiative transfer equation (RTE), which characterizes the propagation of radiation along a specific direction **s** through a medium. The left-hand side of Equation (6) represents the spatial variation of radiative intensity within the medium, whereas the first term on the right-hand side accounts for the local change of thermal radiation due to particle absorption a_p (1 m^{-1}). The second term represents particle emission E_p, in units of (W m^{-3}). This formulation is obtained by neglecting gas-phase emission and absorption and by assuming a zero scattering coefficient. The particles are assumed to act as diffuse emitters, with their radiative emission contributing equally to the intensity in all directions. Consequently, the particle emission E_p is normalized by 4π. The term $I_{(\mathbf{s},\,\mathbf{r})}$ denotes the radiation intensity (W m^{-2} sr^{-1}) at position **r** and along direction **s**. To determine $I_{(\mathbf{s},\,\mathbf{r})}$, and subsequently the incident radiation G (W m^{-2}), the DOM solves a predetermined set of RTEs corresponding to prescribed discrete directions. In the present study, the angular space in each quadrant is discretized using three azimuthal angles and four polar angles. This angular discretization results in a total of 48 RTEs being solved for the three-dimensional radiation field. The radiation balance for an individual CFD cell results in the discretized formulation of the RTE (Equation 7), where $\mathbf{S} = \mathbf{s}\omega_i$, with ω_i being the discrete solid angle associated with a specific direction i. In addition, the net radiative heat flux to the particles within the system is expressed in Equation (8), which assumes that each particle is exposed to a spatially homogeneous radiation field:

$$(\nabla \cdot I_{(\mathbf{s},\,\mathbf{r})}) \cdot \mathbf{s} = -a_p\, I_{(\mathbf{s},\,\mathbf{r})} + \frac{E_p}{4\pi} \tag{6}$$

$$\sum_{i}^{N_{\text{ray}}} \sum_{\text{face}} I_{\text{face},i} \mathbf{S} A_{\text{face}} = -a_p\, \omega_i I_{\text{cell},i} + \frac{E_p}{4\pi} \omega_i \tag{7}$$

$$\begin{aligned} \dot{Q}_{\text{net rad. } D-P} &= \dot{Q}_{\text{absorbed rad, } p} - \dot{Q}_{\text{emitted rad, } p} \\ &= \epsilon_{\text{rad},p} \phi A_p \left(\frac{G_{\text{cell}}}{4} - \sigma T_p^4 \right) \end{aligned} \tag{8}$$

where ϕ is the local bed porosity, $\epsilon_{\text{rad},p}$ is the emissivity of the particle, σ is the Stefan–Boltzmann constant, and A_{face} is the area of one side of a cell. a_p and E_p are computed based on:

$$a_p = \frac{1}{V_{\text{cell}}} \phi \sum_{i=1}^{N} \epsilon_{\text{rad},p} A_{\text{Proj},i} \tag{9}$$

$$E_p = \frac{1}{V_{\text{cell}}} \phi \sum_{i=1}^{N} \epsilon_{\text{rad},p} A_{p,i} \sigma T_{p,i}^4 \tag{10}$$

where V_{cell} is the CFD cell volume, and $A_{\text{Proj},i}$ denotes the area of the particle projected in the i^{th} direction ($A_{\text{Proj},i} = \pi R^2$).

To ensure physical consistency, the absorption and emission terms introduced in the RTE must be reflected in the net radiative heat flux exchanged between the discrete particles and the radiation field, $\dot{Q}_{\text{net rad } D-P}$. Accordingly, the formulation maintains a balance between the emission and absorption terms in the RTEs and the heat balance $\dot{Q}_{\text{net rad } D-P}$ applied to each Lagrangian particle. The absorption coefficient, a_p, depends on the number of particles N within a CFD cell, implying that increased particle number leads to enhanced radiative absorption within the cell and implicitly accounts for shadowing effects at the cell scale. As indicated by Equation (7), the influence of particles on radiation transport through a cell is incorporated by appropriately defining the absorption and emission terms, a_p and E_p. In the present work, these parameters are adjusted based on the local porosities and particle number, allowing different packing densities and locally time-varying porosities/particle numbers to be accounted for.

The DOM heat transfer model has been validated in our previous publication [10] by comparison with simulations employing the P1 radiation model by Mačak et al. [16] and corresponding experimental measurements conducted by De Beer [17]. The validation setup consists of a vacuum-filled enclosure containing 332 spherical graphite particles of radius 0.03 m, positioned between two isothermal graphite walls, one maintained at high and the other at low temperature. Two validation cases are considered: one involving radiative heat transfer only, and a second accounting for the combined effects of radiation and conduction. For the radiation-only case, the steady-state particle temperature distribution predicted by the DOM shows close agreement with the P1 model results. When conduction is included, particle temperatures increase slightly near the high-temperature wall and decrease markedly near the low-temperature wall relative to the radiation-only solution. In this case, the numerical predictions exhibit strong agreement with experimental data, demonstrating the capability of the present model to accurately capture coupled radiative and conductive heat transfer in packed particle systems. Further information on this validation case and the DOM model employed are available in our earlier publication [10].

2.5 | Model for Intra-Particle Calcination

A radially resolved model is used to track the conversion of limestone to quicklime. By discretizing a spherical particle into 40 radial CVs (shells), the internal temperature distribution and reaction kinetics are solved. The particle's outer diameter remains constant, which is a reasonable assumption for limestone. The calcination degree is the ratio of the CO_2 released to the initial amount of CO_2 bound in $CaCO_3$.

$$D_{\text{calcination},p} = \frac{m_{CaCO_3} - m(t)}{m_{CaCO_3} - m_{CaO}} \tag{11}$$

where m_{CaCO_3} is the initial mass of $CaCO_3$, $m(t)$ is the time-varying particle mass, and m_{CaO} is the mass of CaO corresponding to fully calcined particles. The porosity of each shell, ε_s, is determined by considering the solid molar volumes V_m, the initial porosity of the limestone ε_{CaCO_3}, and the reaction progress rp_s:

$$\varepsilon_s = \varepsilon_{CaCO_3} + \left(1 - \frac{V_{m,CaO}}{V_{m,CaCO_3}}\right)\left(1 - \varepsilon_{CaCO_3}\right) rp_s \tag{12}$$

The reaction progress ranges from zero to one, indicating the extent of the calcination. It is mathematically defined as the ratio of the mass of calcium oxide ($m_{s,CaO}$) formed at any given stage to the total mass of calcium oxide that would be produced upon complete calcination:

$$rp_s = \frac{m_{s,CaO}}{(1 - \varepsilon_{CaO})\,\rho_{CaO}\,V_s} \tag{13}$$

where V_s is the shell volume, ρ_{CaO} is the lime density, and ε_{CaO} is the porosity of lime. The porosity of lime (ε_{CaO}) is calculated from Equation (13) by setting the reaction progress (rp_s) to 1, ensuring that it corresponds to the fully reacted state of the material.

The energy balance for a particle is given by Equation (14). At this stage, it is considered that the shell's solid temperature is in thermal equilibrium with the gas temperature within its pores, primarily due to the large surface area. It is also crucial to highlight that heat sources from convection, surface contact, and radiation are only applied to the outermost shell (CV).

$$V_s\,\rho_s c_{p,s}\,\frac{\partial T_s}{|\partial t|} = A_j\,k_j \nabla T_s + \dot{Q}_{conv} + \dot{Q}_{net\ rad\ D-P} + \dot{Q}_{contact} + \dot{Q}_{r,s} \tag{14}$$

where $c_{p,s}$ is the shell specific heat capacity, $\dot{Q}_{r,s}$ represents the heat generated by the reaction in each shell, and the subscript j denotes the boundary separating two adjacent CVs, where interpolation based on CV values is utilized, with the exception of the area A_j. The rate of CO_2 release in each shell is obtained based on:

$$\frac{dn_{CO_2,s}}{dt} = A_{r,s}\,k'_{r,s}\,\left(c_{CO_2,s} - c_{CO_2,eq}\right) \tag{15}$$

where $A_{r,s}$ is the shell area of reaction, and $k'_{r,s}$ is the reaction rate. The CO_2 concentration, $c_{CO_2,s}$, is:

$$c_{CO_2,s} = \frac{\rho_{gas,s}\ \cdot\ Y_{CO_2,s}}{M_{CO_2}} \tag{16}$$

The equilibrium CO_2 concentration, $c_{CO2,eq}$, is also temperature-dependent:

$$c_{CO_2,eq} = \frac{1}{R_m T_s}\left(101325 \cdot \exp \times \left(17.74 - 0.00108T_s + 0.332\ln\left(T_s\right) - \frac{22020}{T_s}\right)\right) \tag{17}$$

where R_m is the universal gas constant. The associated reaction rate is defined by an Arrhenius-type expression:

$$k'_{r,s} = K_0\,T_s^{\,b}\,e^{-\frac{E_a}{R_m T_s}}\,K_{T,c} \tag{18}$$

where the activation energy is $E_a = 33.474$ kJ mol^{-1}, the temperature exponent is $b = 1$, and the pre-exponential factor is $K_0 = 10^{-4}$ m s^{-1} K^{-1}. The term $K_{T,c}$ represents a correction factor, as described in Ref. [5]:

$$K_{T,c} = \begin{cases} 2.5, & T_s < 1150\,K \\ \frac{480}{T-958}, & T_s \geq 1150\,K \end{cases} \tag{19}$$

Equation (15) shows that higher T accelerates reaction rate via the Arrhenius term, and higher CO_2 concentrations slow down calcination by reducing the driving force for CO_2 to diffuse from within the particle and by shifting the equilibrium toward $CaCO_3$ formation.

Assuming that air and carbon dioxide are the only gaseous components present inside the particle, the transport equations, in their spatially discretized form, are then expressed as:

$$\varepsilon_s\,V_s\,\frac{\partial \rho_{gas,s}}{\partial t} = -\sum\left(\varepsilon_s\,\rho_{gas,j}A_j v'_j\right) + M_{CO_2}\frac{dn_{CO_2,s}}{dt} + S_{gas} \tag{20}$$

$$\varepsilon_s V_s \frac{\partial\left(\rho_{gas,s}\,Y_{CO_2,\,s}\right)}{\partial t} = -\sum\left(\varepsilon_s \rho_{gas,j}\,A_j\left(v'_j Y_{CO_2,\,s} - D_{CO_2}\nabla Y_{CO_2,\,s}\right)\right) + M_{CO_2}\frac{dn_{CO_2,s}}{dt} + S_{CO_2} \tag{21}$$

where M_{CO_2} is the molecular weight of CO_2, $n_{CO_2,s}$ is the number of moles of CO_2 in shell s. The advection velocity v'_j is calculated based on Darcy's law for flow through porous media, as described in Ref. [5]:

$$v'_j = -\frac{\kappa}{\mu_{gas,j}}\nabla p \tag{22}$$

The permeability κ is a model parameter, whereas the viscosity μ_{gas} is computed by weighting the viscosities of air and CO_2 according to their respective mass fractions. The pressure is then determined using the ideal gas law.

The diffusion term governs the transport of the generated CO_2 both inward and outward. The diffusion coefficient is evaluated at the interface between two adjacent shells, considering the effective diffusion coefficient $D_{eff,k}$ for the components $k = \{CaCO_3, CaO\}$ within the porous structure and the reaction progress [5]:

$$D_{CO_2} = rp_s D_{eff,CaO} + (1 - rp_s)\,D_{eff,CaCO_3} \tag{23}$$

$$D_{eff,k} = \frac{\varepsilon_k}{\psi_k^2\left(\frac{1}{D_{CO_2,air}} + \frac{1}{D_{Kn,k}}\right)} \tag{24}$$

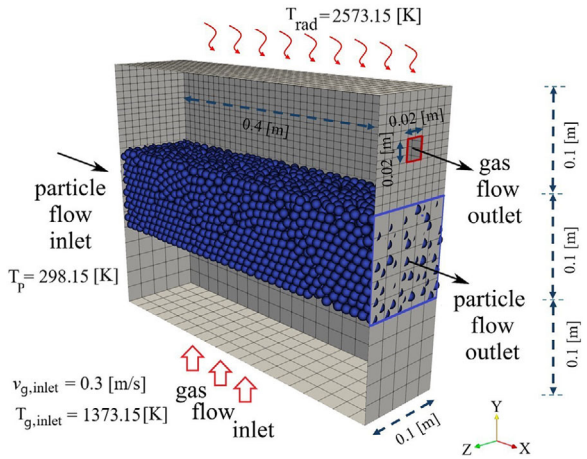

FIGURE 1 | The meshed domain and boundary conditions. Reproduced from Abdi et al. [10], licensed under CC BY 4.0.

where ψ represents the tortuosity, and $D_{CO_2,air}$ and D_{Kn} denote the binary and the Knudsen diffusion coefficients, respectively.

The calcination model has been validated in our previous paper [5] using experimental measurements for a single spherical particle.

2.6 | DEM–CFD Coupling Routine

Momentum exchange is modeled using a one-way coupling, where the particle bed affects the gas flow without feedback on particle motion. The superficial gas velocity is approximately 5% of the minimum fluidization velocity, placing the system well within the fixed-bed regime. Under these conditions, gas-phase drag forces are significantly smaller than gravitational and contact forces acting on the particles and are therefore insufficient to alter particle trajectories or induce bed restructuring. The influence of gas-phase momentum on particle motion can thus be considered negligible, justifying the use of a one-way momentum coupling approach. Furthermore, particle velocities are prescribed and the DEM mechanical motion equations are not solved, rendering two-way momentum coupling physically redundant within the present modeling framework. In contrast, thermal and species transport processes are strongly governed by local gas–solid interactions and radiative heating of particles; hence, a two-way coupling is retained for energy and mass transfer. Details on the DEM–CFD coupling approach are available in [18].

3 | Simulation Setup

The computational domain employed in this study is adapted from our previous work [10]. It consists of a box with dimensions $0.4 \times 0.3 \times 0.1$ m^3, as illustrated in Figure 1, and is discretized into 6200 hexahedral elements. Mesh size in the bulk region is $0.02 \times 0.02 \times 0.02$ m^3. Finer mesh elements are applied in the upper section of the domain.

Air (comprising 23% O_2 and 77% N_2 by mass) enters the system through the bottom surface with a velocity of 0.3 m s^{-1}, a temperature of 1373.15 K, and a thermal conductivity of 0.04 W m^{-1} K^{-1}. It exits via a small outlet (0.02×0.02 m^2), positioned at the top right boundary of the box, highlighted in red in Figure 1.

Particles flow through the left boundary (0.1×0.1 m) at 298.15 K and exit via the right outlet. The outlet boundary has a zero-gradient condition for both velocity and temperature, and the outlet pressure is set to atmospheric (zero relative gauge pressure). A no-slip condition is applied to all walls, which are assumed to be adiabatic with respect to convection. Additionally, the top wall is maintained at a fixed temperature of 2573.15 K (T_{rad}), whereas the remaining walls are kept at 298.15 K. The emissivity of the top wall ε_{rad} and the absorptivity a_w are both 0.7, whereas for all other walls, the values are 1.

Three random particle configurations—dilute (540 spheres), moderate (2560 spheres), and dense (5000 spheres)—were examined, with corresponding average porosities in the particle zone of 93%, 66.5%, and 34.5%, respectively. In fluid simulations, local porosity values are applied at the cell level rather than using these global averages. The particle arrangements are created as follows: Initially, 5000 spheres are randomly introduced into the domain through a DEM simulation by dropping them from the top. To generate the moderate and dilute configurations, approximately half and then another 2000 spheres are randomly removed, respectively. For details, see also [10].

Each configuration maintains same particle velocities and residence times but differs in solid mass flow rates. In all configurations, particles are assigned a constant velocity of 0.0002 m s^{-1} along the x-axis. The residence time for a particle to travel from the left to the right boundary, $t_{residence}$, is 2000 s.

3.1 | Simulation Parameters

Table 1 presents the parameters used in the DEM–CFD simulations. The limestone density is 2812.05 kg m^{-3} without pores and 2700 kg m^{-3} when pores are included. During calcination, particle volume is assumed constant, and as a result, their density decreases.

4 | Results

In the following, results are presented for three different particle configurations, referred to as the dilute (540 spheres), the moderate (2560 spheres), and the dense (5000 spheres) configurations. Simulations for each configuration are performed both with and without calcination (i.e., using inert particles with a density of 2700 kg m^{-3}), referred to as the calcined and uncalcined cases, respectively. For the discussion, it is important to keep in mind that calcination begins as soon as the particle temperatures reach the threshold for this endothermic reaction, which is around 800–900°C, and the reaction rate increases exponentially with temperature. In addition to temperature, according to Equation (15), the reaction rate of lime particles is also governed by the local CO_2 mass fraction.

TABLE 1 | Simulation parameters.

Parameter	Unit	Value
CFD time step	(s)	0.0002
DEM time step	(s)	0.001
Gas absorption coefficient	(m^{-1})	0
Gas emissivity	(—)	0
Gas inlet velocity	(m s^{-1})	0.3
Gas thermal conductivity	(W m^{-1} K^{-1})	0.04
Particle diameter	(mm)	10
Particle emissivity	(—)	0.85
Particle initial mass	(g)	1.413
Particle Poisson's ratio	(—)	0.35
Particle residence time	(s)	2000
Particle velocity	(m s^{-1})	0.0002
Particle Young's modulus	(Pa)	1.0×10^9
$CaCO_3$ properties		
Density (without pore)	(kg m^{-3})	2812.05
Heat capacity	(J $kg^{-1}K^{-1}$)	836.8
Molar mass	(kg mol^{-1})	0.1
Porosity	(—)	0.04
Solid conductivity	(W $m^{-1}K^{-1}$)	2.26
Specific surface area	(m^2 kg^{-1})	16 000.0
Tortuosity	(—)	1.4142
Permeability	(m^2)	5×10^{-15}
CaO properties		
Density (without pore)	(kg m^{-3})	3310.0
Heat capacity	(J kg^{-1} K^{-1})	753.1
Molar mass	(kg mol^{-1})	0.056
Porosity	(—)	0.543
Solid conductivity	(W m^{-1} K^{-1})	0.7
Specific surface area	(m^2 kg^{-1})	7000.0
Tortuosity	(—)	1.4142
Permeability	(m^2)	5×10^{-15}

4.1 | Radiation Field

To facilitate the interpretation of the results, the main radiative heat transfer mechanisms within the particle bed are briefly outlined. Radiation emitted by the high-temperature top wall heats particles that are directly visible to the wall. These are mainly particles located in the upper layer of the bulk. However, depending on the local packing porosity, radiation may also penetrate deeper into the bed and reach lower particle layers. A more dispersed particle arrangement, characterized by larger void spaces, allows radiation to penetrate directly to deeper layers. In our previous study [10], considering a radiation-only scenario while neglecting convection, conduction, and calcination, we showed that the dilute configuration exhibits the largest "direct" radiation penetration depth due to its higher void fraction.

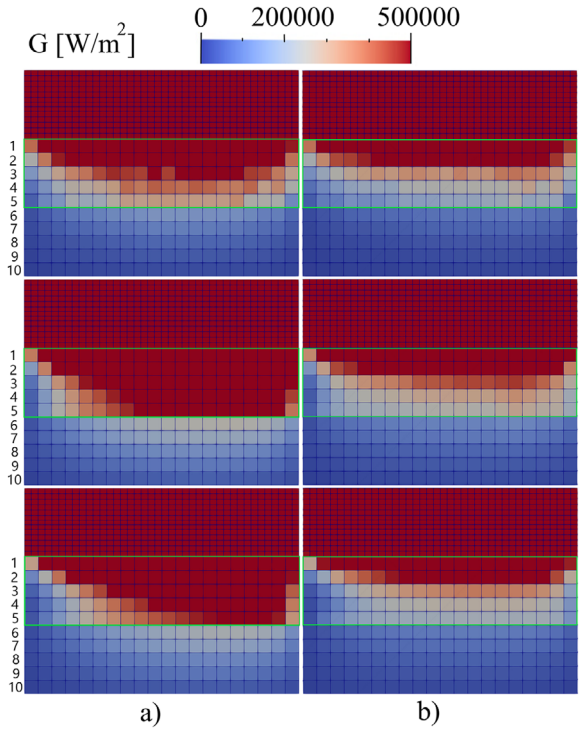

FIGURE 2 | Incident radiation G (W m^{-2}) contour in the configuration of dilute (top), moderate (middle), and dense (bottom). (a) Uncalcined and (b) calcined (G clipped above 500 000 W m^{-2}).

As the temperature of particles in the upper layers increases, these particles emit thermal radiation and contribute to the heating of particles located in the layers below. Consequently, a radiative heating front gradually propagates downward through the bulk. For the denser configurations, radiation absorption in the top layers and its subsequent re-emission toward lower layers become more important (hereafter referred to as the "layer-emission mechanism"), where direct radiation is strongly limited by particle shadowing. In addition, particles can emit radiation to neighboring particles within the same layer, resulting in a "horizontal spread" of radiative heat transfer. This horizontal radiation spread is also most pronounced in the dilute configuration due to the larger void spaces between particles, which enable radiative transfer between particles over larger distances [10].

Figure 2 illustrates the distribution of incident radiation G within the domain in (W m^{-2}). The spatial magnitude of G depends on the temperatures of the surrounding walls as well as on the local particles/packing properties. Due to the $\sim T^4$ dependence, the high-temperature top wall emits radiation at significantly higher intensities than the side-walls maintained at 298.15 K. The total amount of radiation locally emitted by the packing depends on the local packing density and the particle temperature. Radiation originating from all wall boundaries and the particles is balanced at each position and results in a specific G value. Figure 2a presents the results for uncalcined cases, whereas Figure 2b corresponds to calcined cases. The local values of G indicate the extent to which radiation penetrates the particle bed. The particle-filled region is marked in green, and the rows of fluid cells are numbered from 1 to 10. Furthermore, the average G values for fluid cells in rows 1–10 are plotted in Figure 3.

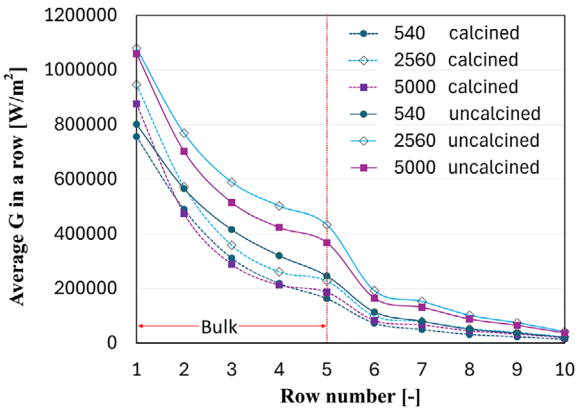

FIGURE 3 | G (W m^{-2}) values averaged over all fluid cells in rows 1–10 of the G contour for dilute (top), moderate (middle), and dense (bottom) configurations. The red dotted line indicates the end of the particle zone.

Figure 3 shows that radiation penetration extends to the fifth row (the end of the particle zone) for all three packing densities and for the calcined and uncalcined cases. A gradient in G from row 6 to row 10 results from radiative interactions between the bottom layer of spheres and the low-temperature walls of the enclosure beneath the particle bed.

Interestingly, although the dilute configuration provides higher direct visibility between particles, Figure 2a indicates that in the uncalcined cases the effective radiation penetration depth is larger in the moderate and dense configurations than in the dilute configuration. This observation can be explained by the layer-emission mechanism. In the moderate and dense configurations, the densely packed top layer absorbs a larger fraction of the incoming radiation from the heated wall. As these particles heat up, they emit more radiation toward the lower layers, thereby enhancing the overall radiation penetration depth.

The moderate configuration exhibits higher G values compared with the dense configuration (Figure 3). This can be attributed to the combined influence of convection and conduction, which shape the overall particle temperature field. As a result, the mean particle temperature is higher in the moderate configuration than in the dense configuration. In the uncalcined case, the mean particle temperatures are 1293.81 and 1238.45 K for the moderate and dense configurations, respectively, whereas in the calcined case, they are 1138 and 1075 K. The higher mean particle temperature in the moderate configuration leads to stronger radiative emission between particles, which further contributes to the higher G values. Overall, the moderate configuration exhibits the largest radiation penetration depth, independent of whether calcination is considered or not.

As mentioned above, calcination causes a drop in particle temperature. As a result, the top particle layers emit less radiation toward the lower layers, leading to a reduced radiation penetration depth as can be seen in Figure 2b. This reduction in particle temperature also results in lower row-averaged G values across all particle rows compared to the uncalcined cases (Figure 3). The dilute configuration is affected less strongly because both direct radiation from the top boundary and inter-layer emission contribute to G. Although layer emission can be significant, direct radiative visibility remains an important mechanism and is largely unaffected by calcination. In contrast, in the moderate and dense configurations, direct radiation is strongly limited by particle shadowing, and radiative transfer is dominated by emission from the upper particle layers. When calcination lowers the temperatures of these layers, their emitted radiation toward the lower layers decreases, thereby weakening this dominant mechanism and reducing the radiation penetration depth more significantly.

4.2 | Radiative and Convective Heat Fluxes

It is also interesting to analyze the heat fluxes delivered to the particles from external sources—namely, convection and radiation—and to determine which heat transfer mechanism dominates. Table 2 shows the heat fluxes due to radiation and convection, summed over all particles for the calcined and uncalcined cases. Furthermore, the net heat (radiation and convection is listed per particle). Obviously, radiation is clearly the dominant mechanism in all calcined cases, with the average radiative heat transferred to the particles being 632, 3727, and 5922 W for the dilute, moderate, and dense configurations, respectively. In contrast, the heat transferred via convection is lower, at 360, 184, and 170 W, respectively. It should be noted that these are average values across all particles, meaning that although some particles lose heat, others gain heat through convection.

Similarly, in the uncalcined cases, radiative heat flux remains dominant over convective heat flux. However, the amount of radiative heat received is lower—more than 2.3 times less—compared to the calcined cases. This difference arises because, in the calcined cases, heat is consumed by the calcination process, resulting in lower particle temperatures and, consequently, higher absorption of radiative heat from the top wall. For the same reason, the lower particle temperatures in the calcined cases also lead to significantly higher convective heat transfer.

Notably, the heat received per particle is highest in the dilute cases, followed by the moderate and dense configurations. For calcination, this suggests a higher degree of calcination in the dilute configuration (see Figure 7).

At first glance, the convection results appear surprising: The dilute configuration shows a higher total convective heat transfer (360 W in the calcined case) than the dense configuration (170 W in the calcined case), despite the denser packing having lower porosity—leading to higher mean gas velocities and, consequently, larger heat transfer coefficients—as well as a much larger number of particles (approximately 10 times more than in the dilute configuration). This behavior is explained by the direction of the convective heat flux, which depends on the local temperature difference between gas and particles. In the dilute configuration, the gas temperature is higher than the particle temperature in most regions, resulting in net convective heating of the particles. In the dense configuration, however, many particles in the upper layers are at a larger temperature than the gas and transfer heat back to it, which reduces the overall net convective heat transfer.

TABLE 2 | Comparison of radiative and convective heat fluxes summed over all particles in calcined and uncalcined cases, along with the net heat flux per particle ($\dot{Q}_{conv} + \dot{Q}_{rad}$).

	Radiative heat flux (W)		Convective heat flux (W)		Net heat flux per particle (W)	
Configuration	**Calcined**	**Uncalcined**	**Calcined**	**Uncalcined**	**Calcined**	**Uncalcined**
Dilute	632	221.4	360	115	1.837	0.623
Moderate	3727	1467	184	7.6	1.527	0.576
Dense	5922	2544	170	80	1.218	0.525

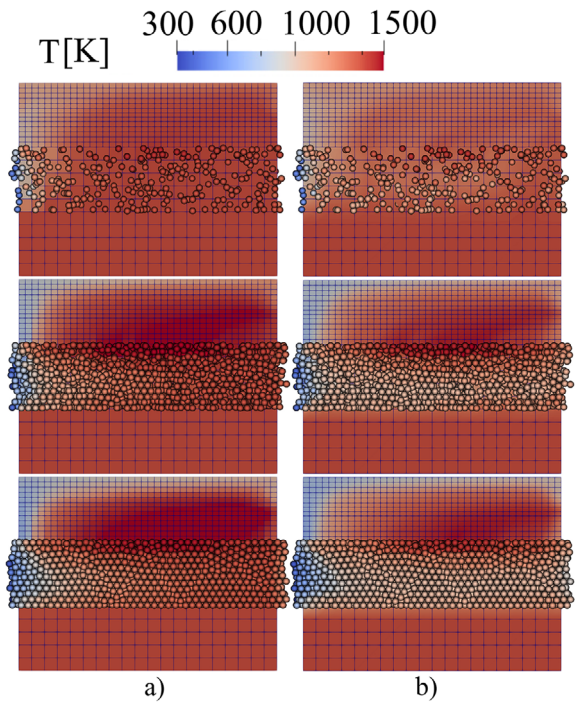

FIGURE 4 | Surface temperature of particles and gas-phase temperature in the configuration of dilute (top), moderate (middle), and dense (bottom). (a) Uncalcined and (b) calcined (clipped at 300 and 1500 K).

4.3 | Temperature Field

Figure 4 shows the temperature fields of both particles and fluid for the uncalcined (Figure 4a) and calcined cases (Figure 4b). For both cases, the highest particle surface temperatures occur in the upper region of the bed, mainly due to radiative heat transfer from the top wall. Furthermore, the particle temperature increases from the inlet to the outlet as particles gradually absorb heat while moving through the system, primarily through convection from the bottom and radiation from the top wall. An exception occurs for particles located in the upper layer near the outlet. These particles already have received strong radiative heating and therefore can lose heat to the surrounding gas by convection, which may result in slightly lower particle temperatures at the outlet compared to particles located further upstream.

Significant temperature variations are observed along the bed height for both the uncalcined and calcined cases. In Figure 4a, the uncalcined particles across the bed appear deep red, indicating relatively high temperatures throughout the bed. In contrast, for the calcined case in Figure 4b, most particles appear brighter, reflecting lower temperatures. This difference arises because, in the calcined case, part of the absorbed heat is consumed by the endothermic calcination reaction. Consequently, the top particle layer is at a relative low temperature, emitting less radiation to the underlying layers, causing particle temperatures to decrease progressively with depth in the bed. As expected, particle temperatures are therefore generally higher throughout the bed in the absence of calcination.

Regarding the gas phase, the temperature above the bulk region is higher in the uncalcined case compared to the calcined cases. This is primarily because the particles at the top receive radiation heat from the top wall, and, without undergoing calcination, they retain more heat and transfer it to the gas through convection.

Figure 5 shows the histograms of particle temperature for three packing densities for both the calcined (I: top) and uncalcined (II: bottom) cases. In each histogram, the left side corresponds to particles at lower temperatures located near the particle inlet, whereas the right side represents particles at higher temperatures, situated near the middle of the top layer.

For the uncalcined cases (II), all configurations exhibit a pronounced peak at the high-temperature end. However, the peak temperature differs slightly between the packing densities, reaching 1367 K for the dilute configuration, 1373.53 K for the moderate configuration, and 1334.71 K for the dense configuration. These peaks correspond primarily to particles located in the right half of the domain. In addition, the fraction of particles at the peak temperature decreases with increasing packing density: 26.6% (dilute), 12.65% (moderate), and 7.68% (dense). This behavior is attributed to the more effective and spatially uniform heat distribution in the dilute configuration. Due to its high porosity, radiation penetrates directly into the bed and a larger number of particles are directly exposed to the high-temperature wall. In addition, the gas retains a significant portion of its enthalpy while flowing through the bed (which will be discussed in Section 4.4), further contributing to particle heating. As a result, many particles reach similar high temperatures, leading to a pronounced peak in the histogram.

In contrast, for the calcined cases (I), the endothermic nature of the calcination reaction significantly alters the temperature distribution. The histogram peaks shift toward lower temperatures, and their magnitudes decrease substantially. The peak temperatures are reduced to 1179 K (dilute), 1063 K (moderate), and 1050 K (dense), with corresponding particle fractions of 5.5%, 7.3%, and 11%, respectively.

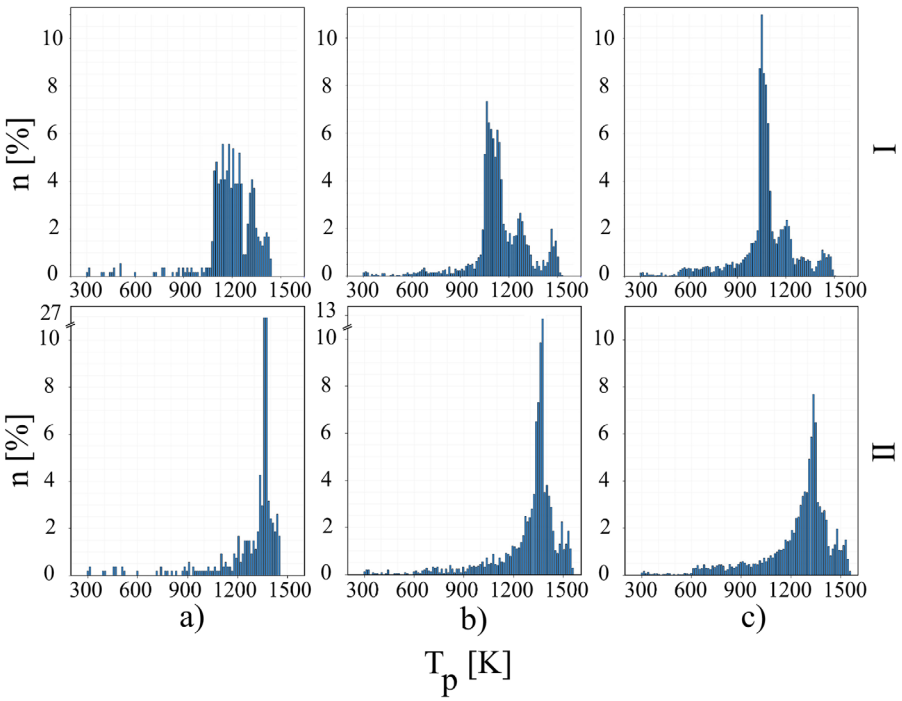

FIGURE 5 | Percentage of particles (relative to the total number of particles in each case) plotted against their surface temperature across the entire domain for the dilute (a), moderate (b), and dense (c) configurations. (I) represents the calcined cases, and (II) represents the uncalcined cases.

The reversal in peak magnitude across packing densities can be explained by the interaction between heat transfer and reactive heat consumption. In the dilute configuration, particles receive the highest heat input per particle (Table 2) and exhibit the highest calcination degree (98%, Figure 7). Consequently, the reaction is highly active and consumes a significant portion of the supplied heat. This results in a broader temperature distribution and a reduced accumulation of particles at a single temperature, hence a much smaller peak. In the dense configuration, heating is dominated by radiation in the upper layers and convection in the lower layers. This leads to a more heterogeneous spatial temperature distribution in the uncalcined case and a smaller peak. However, during calcination, the overall calcination degree is lower (~60%, Figure 7), partly due to nonuniform heat distribution within the bed and higher CO_2 concentrations (which will be discussed in the following section), which inhibit the reaction. As a result, less heat is consumed, and particles behave more similarly to the inert case. This allows temperatures to cluster more strongly around a common value, leading to a relatively higher peak compared to the dilute configuration.

The maximum particle surface temperatures in the uncalcined cases reach 1451, 1555, and 1555 K for the dilute, moderate, and dense configurations, respectively, and occur in the upper layer. In the calcined cases, the maximum temperatures decrease to 1438, 1529, and 1503 K for the dilute, moderate, and dense configurations, respectively, also occurring in the upper layer. The generally lower temperatures observed for the calcined case is attributed to the temperature drop resulting from the endothermic nature of the calcination process. The maximum temperature is lower in the dilute than in the moderate and dense configuration for both calcined and uncalcined cases. This trend in maximum temperature can be explained as follows. In the dense configuration, the gas velocity within the particle bulk increases, which enhances the convective heat transfer coefficient h. Consequently, particles in the bottom layers experience stronger convective heating, and their temperature rises. As a result, they absorb less radiative heat from the high-temperature particles located in the upper layers. This allows the particles in the upper region to increase their temperature further through radiative heat transfer from the hot wall, leading to higher maximum particle temperatures. Although convection removes heat from the top-layer particles by heating the surrounding air above the bed, the radiative heat input to these particles is considerably larger, enabling them to reach higher temperatures than in the dilute configuration.

Interestingly, the standard deviation (SD) for the particle surface temperature is of the same order of magnitude for both uncalcined and calcined cases (uncalcined: SD = 180.5 K, SD = 194.6 K, SD = 214.8 K; calcined: SD = 167.3 K, SD = 178.41 K, SD = 185.3 K for dilute, moderate, and dense configurations), indicating that although calcination lowers the overall temperature level, the SD of the temperature distribution remains comparable across configurations.

4.4 | Calcination Degree of the Lime Particles

Figure 6a presents the average calcination degree of lime particles across all radial shells for the three packing densities. Similar overall trends are observed for all configurations, with high calcination degrees appearing near the upper region of the particle bed. This behavior is mainly attributed to radiative heating from the high-temperature top wall, which raises particle

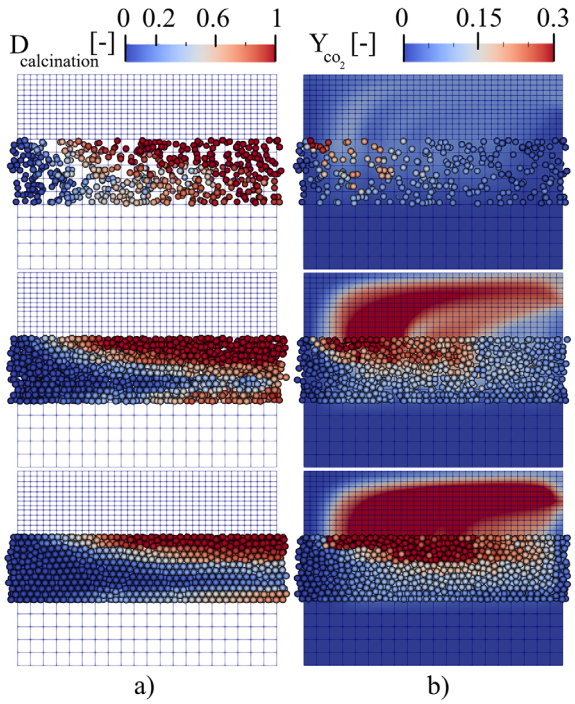

FIGURE 6 | (a) Calcination degree of lime particles and (b) mass fraction of CO_2 in both fluid and solid domains (clipped to 0.3) in dilute (top), moderate (middle), and dense (bottom) configurations.

temperatures above the calcination threshold. In addition to the upper region, significant calcination is also observed in the lower part of the bed. This is primarily caused by convective heat transfer from the incoming high-temperature gas, which supplies the energy required for the endothermic calcination reaction. Spatially nonuniform calcination is observed across all three packing densities, with unreacted zones consistently appearing in the middle layers of the particle bed and near the particle inlet. For the middle layers, this uneven calcination arises because particles in these layers receive neither sufficient radiation from the top wall nor adequate convective heat transfer from the bottom, preventing them from reaching the calcination temperature. Near the inlet, particles have not reached the calcination threshold.

When an unreacted core exists, zones with high calcination degrees naturally develop near the top and bottom regions of the bed. However, the extent of these high-calcination zones decreases as the bed becomes denser (i.e., as bed porosity decreases). Several factors contribute to this behavior:

One important factor is the variation in convective heat transfer and *G* penetration within the particle bed. As the packing density increases, the convective heat transfer coefficient *h* also increases, leading to stronger heat transfer from the gas to the particles in the lower layers. In the dense configuration, the incoming gas transfers most of its thermal energy to the particles in the bottom layer, causing rapid calcination there. Consequently, little thermal energy remains in the gas to heat the upper layers. In the moderate configuration, part of the gas enthalpy remains available to heat the particles in the second layer from the bottom, whereas the deeper *G* penetration compared to dense

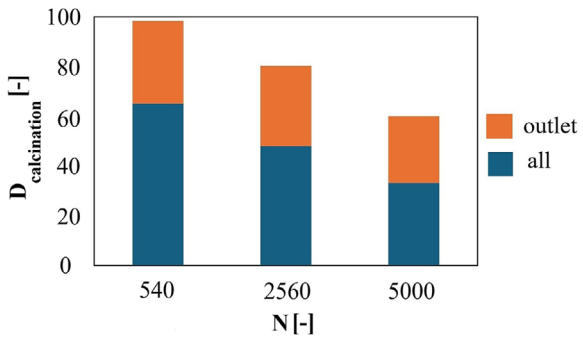

FIGURE 7 | Average calcination degree for outlet (orange) and all (blue) lime particles.

configuration (Figure 3) also promotes calcination in the middle layers. This leads to an expansion of both the lower and upper calcination zones compared to the dense configuration. The dilute configuration allows for a larger fraction of the gas enthalpy to remain available as the gas moves upward through the bed. Combined with radiative heating from the top wall, this leads to the highest overall calcination levels in both the upper and lower regions of the particle bed.

Another important factor is the concentration of CO_2 in the gas phase (Figure 6b). The CO_2 concentration is lowest in the dilute configuration and increases in the moderate and dense configurations. Since higher CO_2 partial pressure suppresses calcination, this effect reduces the degree of calcination in the upper layers of the denser beds.

As can be seen in Figure 7, the simulation yields average calcination degrees of 98%, 80%, and 60% for particles at the outlet in the dilute, moderate, and dense configurations, respectively, whereas the average calcination degrees for all particles are 65%, 48%, and 33%. These results demonstrate that the average calcination degree decreases with increasing packing density. This trend is primarily attributed to the CO_2 concentration in the gas phase, as well as variations in convective and radiative heat transfer within the bed, as discussed above, and scales roughly with the heat received per particle by convection and radiation as listed in Table 2.

Figure 8 illustrates the percentage of particles (relative to the total particle in each case) plotted against their average calcination degree across the entire domain for the dilute (a), moderate (b), and dense (c) configurations. As observed, 27%, 19.4%, and 10.7% of particles are fully calcined in the dilute, moderate, and dense configurations, respectively. Conversely, about 8%, 13.4%, and 22% of particles remain completely uncalcined in the dilute, moderate, and dense configurations, respectively.

4.5 | CO_2 Mass Fraction

Figure 6b illustrates the CO_2 mass fraction in both the fluid and solid domains for each simulation case. As the particles enter the system with a uniform initial temperature of 298.15 K, no calcination occurs at the inlet and therefore no CO_2 is initially produced inside the particles. As the particles move through the

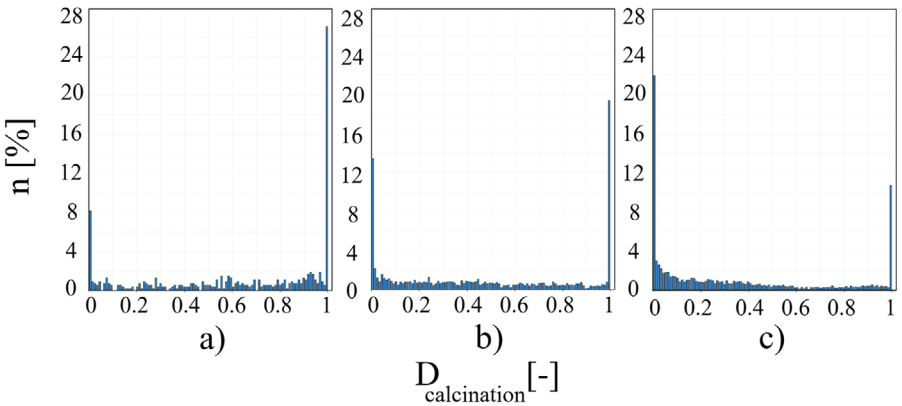

FIGURE 8 | Percentage of particles (relative to the total number of particles in each case) plotted against their average calcination degree across the entire domain for the dilute (a), moderate (b), and dense (c) configurations.

bed, they gradually absorb heat, which initiates the calcination reaction and leads to the release of CO_2 to the gas phase.

Near the inlet, several particles in the top layer appear red, indicating a high CO_2 content within the particles. As these particles move toward the outlet, their color gradually changes from red to orange and eventually to blue, reflecting the progressive release of internal CO_2 into the gas phase. Consequently, the red particles observed in the top layer of Figure 6a correspond to orange particles (partially calcined) and blue particles (fully calcined, with negligible remaining CO_2) in Figure 6b.

The spatial distribution of CO_2 in both the gas and solid phases reveals clear differences between the packing configurations. In the dilute configuration, calcination occurs very rapidly and is largely completed within approximately the first one-fifth of the domain. For the moderate configuration, most of the CO_2 is concentrated in the left half of the domain, indicating that the calcination reaction primarily occurs in this region. In the dense configuration, CO_2 is distributed over a larger portion of the bed, extending to roughly two-thirds of the domain length, which indicates that the calcination reaction progresses more gradually along the bed.

Moreover, Figure 6b shows the accumulation of CO_2 in the gas phase in the fluid domain above the bed, resulting from the decomposition of limestone. The amount of CO_2 in the fluid domain is highest in the dense configuration due to the higher number of particles and, consequently, a larger amount of CO_2 released on the upper side of the bed. This is higher than in the moderate configuration, which in turn is higher than in the dilute configuration. Therefore, although the overall calcination degree is lower in the dense configuration, the influence of particle number is the dominant factor on the gas-phase CO_2 concentration.

5 | Summary and Conclusion

This study investigates the calcination behavior of limestone particles in a moving packed bed, with particular focus on the role of packing density and its interaction with heat transfer mechanisms. A comparison between calcined and uncalcined cases is also performed. A DOM is used in a coupled DEM–CFD framework to model radiative heat transfer within systems of granular particles. The AVM was used to account for particle presence through time-dependent source terms and a porosity field in the Navier–Stokes equations. By incorporating local bed porosity into the modeling of radiative emission and absorption, the simulations capture the influence of packing structure on heat transfer.

A numerical test case was designed to analyze the interaction between a high-temperature wall, a moving particle bed with prescribed velocity, and a cross-flow of high-temperature gas. Spherical limestone particles were heated by radiation from a top wall at 2573.15 K and by convection from air at 1373.15 K, with an inlet velocity of 0.3 m s^{-1}. Conductive heat transfer between particles was also considered. Three packing configurations were studied—dilute (93% porosity), moderate (66.5%), and dense (34.5%)—corresponding to 540, 2560, and 5000 particles, respectively, all with a residence time of 2000 s.

The results demonstrate that packing density strongly governs radiative heat transfer through two competing mechanisms: direct radiation (visibility effect) and layer-emission. In beds with high porosity (i.e., dilute configurations), the large void spaces enhance particle visibility, allowing radiation from the high-temperature top wall to penetrate deeply to the lower particle layers. This high visibility also enables radiation to propagate laterally between particles. As the porosity decreases (i.e., moderate and dense configurations), particle shadowing limits direct radiation, and radiative transfer becomes dominated by absorption in upper layers followed by re-emission toward deeper regions. This layer-emission mechanism enhances the effective radiation penetration depth in moderate and dense configurations, despite reduced direct visibility. Although layer emission also contributes significantly in dilute systems, direct radiation remains a dominant heat transfer mechanism in this configuration.

When calcination is considered, the resulting decrease in particle temperatures weakens the layer-emission mechanism, leading to lower radiation penetration depths and smaller differences between packing configurations. However, the dilute configuration is less affected because direct radiative visibility still

contributes to the heat transfer process. It was observed that, with increasing particle number, the highest calcination degrees become concentrated in the upper and lower regions of the particle bed. The upper layers receive intense radiative heating from the high-temperature wall, whereas the lower layers are primarily heated by convective heat transfer from the incoming gas, which is at high temperature. In contrast, intermediate regions exhibit limited calcination because particles receive insufficient thermal energy from either source.

The average calcination degree decreases with increasing packing density, as the net heat transfer by radiation and convection per particle is reduced. The simulation results yield average calcination degrees of 98%, 80%, and 60% for outlet particles in the dilute, moderate, and dense configurations, respectively.

In summary, this study highlights the critical role of bed porosity in controlling radiation transport and calcination performance in moving particle systems. The balance between direct radiation and layer-emission mechanisms is strongly dependent on packing structure and is further influenced by the inclusion of calcination. These findings provide valuable insight for the design and optimization of high-temperature thermochemical reactors, particularly those in which radiative heat transfer plays a dominant role.

Nomenclature

Symbols

a	absorption coefficient, 1 m^{-1}
A	area, m^2
A_s	specific surface area, m^2 kg^{-1}
$A_{r,s}$	shell area of reaction, m^2
c_p	specific heat capacity, J kg^{-1} K^{-1}
c	molar concentration, mol m^{-3}
d	particle diameter, m
D	diffusion coefficient, m^2 s^{-1}
$D_{\text{calcination}}$	calcination degree, —
D_{Kn}	Knudsen diffusion coefficients, m^2 s^{-1}
E	emission, W m^{-3}
E_a	activation energy, kJ mol^{-1}
G	incident radiation, W m^{-2}
g	acceleration due to gravity, m s^{-2}
h	specific enthalpy, J kg^{-1}
I	radiation intensity, W m^{-2} sr^{-1}
k	thermal conductivity, W m^{-1} K^{-1}
K_0	pre-exponential factor, m s^{-1} K^{-1}
$k'_{r,s}$	reaction rate, m s^{-1}
$K_{T,c}$	correction factor, —
m	mass, kg
$\dot{m}$	mass flux, kg s^{-1}
M_{CO_2}	molar mass of CO_2, kg mol^{-1}
$n_{CO_2,s}$	number of moles of CO_2 generated by reaction in shell s, mol
n	unit normal vector, —
N	number of particles, —
p	pressure (relative to atmospheric pressure), Pa
$\dot{Q}$	heat rate, J s^{-1}
R_m	universal gas constant, J mol^{-1} K^{-1}
r	ray position vector, m
rp_s	reaction progress, —
s	ray direction vector, —
S_M	source term to represent the momentum exchanged between the phases, kg m^{-2} s^{-2}
S_E	source term to represent the enthalpy exchange, W m^{-3}
S_{CO_2}	source term to represent the release of CO_2 from the particles, kg m^{-3} s^{-1}
t	time, s
$t_{\text{residence}}$	residence time, s
T	temperature, K
u	velocity, m s^{-1}
u_{spheres}	spheres velocity, m s^{-1}
$u_{g,\text{inlet}}$	gas velocity at the inlet, m s^{-1}
V	volume, m^3
V_m	solid molar volumes, m^3 mol^{-1}
v'_j	advection velocity, m s^{-1}
y	Young's modulus, Pa
Y_{CO_2}	CO_2 mass fraction, —

Greek Variables

α	heat transfer coefficient, W m^{-2} K^{-1}
ε	intra-particle porosity (porosity inside a porous particle, used in DEM), —
ε_{rad}	emissivity, —
κ	permeability, m^2
μ_{gas}	viscosity, Pa s
ν_p	particle Poisson's ratio, —
ρ	density, kg m^{-3}
σ	Stefan–Boltzmann constant, W m^{-2} K^{-4}
τ	stress tensor, Pa
ψ	tortuosity, —
ϕ	local bed porosity (void fraction in a CFD cell), —
ω_i	discrete solid angle, sr

Sub- and Superscripts

cell	cell
conv	convection
CV	control volume
D–P	enclosure domain and the particles

eff	effective
eq	equilibrium
f	fluid
face	face
g	gas
i	direction index
j	index denoting the boundary between two adjacent control volumes
net	net value
n	normal
p	particle
Proj	projected
rad	radiation
r,s	reaction of each shell
s	shell
t	tangential
w	wall

Acknowledgments

This work has been funded by the Deutsche Forschungsgemeinschaft (DFG, German Research Foundation)—Project-ID 422037413—TRR 287.

Open access funding enabled and organized by Projekt DEAL.

Data Availability Statement

The data that support the findings of this study are available from the corresponding author upon reasonable request.

References

1. R. Abdi, M. Krzaczek, and J. Tejchman, "Simulations of High-Pressure Fluid Flow in a Pre-Cracked Rock Specimen Composed of Densely Packed Bonded Spheres Using a 3D CFD Model and Simplified 2D Coupled CFD-DEM Approach," *Powder Technology* 417 (2023): 118238, https://doi.org/10.1016/j.powtec.2023.118238.

2. R. Abdi, M. Krzaczek, and J. Tejchman, "Comparative Study of High-Pressure Fluid Flow in Densely Packed Granules Using a 3D CFD Model in a Continuous Medium and a Simplified 2D DEM-CFD Approach," *Granular Matter* 24 (2022): 1–25, https://doi.org/10.1007/s10035-021-01179-2.

3. B. Krause, B. Liedmann, J. Wiese, S. Wirtz, and V. Scherer, "Coupled Three Dimensional DEM–CFD Simulation of a Lime Shaft Kiln—Calcination, Particle Movement and Gas Phase Flow Field," *Chemical Engineering Science* 134 (2015): 834–849, https://doi.org/10.1016/j.ces.2015.06.002.

4. B. Krause, B. Liedmann, J. Wiese, et al., "3D-DEM-CFD Simulation of Heat and Mass Transfer, Gas Combustion and Calcination in an Intermittent Operating Lime Shaft Kiln," *International Journal of Thermal Sciences* 117 (2017): 121–135, https://doi.org/10.1016/j.ijthermalsci.2017.03.017.

5. E. Illana, H. Merten, S. Wirtz, and V. Scherer, "DEM/CFD Simulations of a Generic Oxy-Fuel Kiln for Lime Production," *Thermal Science and Engineering Progress* 45 (2023): 102076, https://doi.org/10.1016/j.tsep.2023.102076.

6. S. Duan, B. Li, and W. Rong, "Numerical Simulation Study of Mixed Particle Size Calcination Processes in the Calcination Zone of a Parallel Flow Regenerative Lime Kiln," *Materials* 15 (2022): 4609, https://doi.org/10.3390/ma15134609.

7. R. Abdi, B. Jaeger, T. Bergold, E. Illana, M. Schiemann, and V. Scherer, "Influence of packing density on the calcination process for lime production: A DEM-CFD study," *The 19th International Conference on Fluid Flow Technologies (CMFF'25)*, (Budapest, Hungary, 2025).

8. L. Mieg, T. Bergold, E. Illana, V. Scherer, and M. Mönnigmann, "A Reduced Model for Particle Calcination for Use in DEM/CFD Simulations," *Particuology* 93 (2024): 316–327, https://doi.org/10.1016/j.partic.2024.07.004.

9. E. Illana, K. Qyteti, M. Scharnowski, M. Brömmer, S. Wirtz, and V. Scherer, "Shape-Changing Particles for Locally Resolved Particle Geometry in DEM Simulations," *Particuology* 89 (2024): 185–190, https://doi.org/10.1016/j.partic.2023.11.003.

10. R. Abdi, B. Jaeger, E. Illana, S. Wirtz, M. Schiemann, and V. Scherer, "Modelling of Heat Transfer in Moving Granular Assemblies With a Focus on Radiation Using the Discrete Ordinate Method: A DEM-CFD Approach," *Particuology* 100 (2025): 78–94, https://doi.org/10.1016/j.partic.2025.02.024.

11. Bulk Reaction, "Bulk Reaction Official Website," accessed April 11, 2026, https://bulk-reaction.de/.

12. OpenCFD Ltd., "OpenFOAM v2012 Documentation Guides," accessed April 11, 2025, https://www.openfoam.com/documentation/guides/v2012/doc/.

13. S. Ergun and A. A. Orning, "Fluid Flow Through Randomly Packed Columns and Fluidized Beds," *Industrial & Engineering Chemistry* 41 (1949): 1179–1184, https://doi.org/10.1021/ie50474a011.

14. R. Abdi, M. Krzaczek, and M. Abdi, "From Darcy to Turbulent Flow: Investigating Flow Characteristics and Regime Transitions in Porous Media," *Physics of Fluids* 36 (2024): 103372, https://doi.org/10.1063/5.0232176.

15. N. Hilse, M. Kriegeskorte, J. Fischer, et al., "Discrete Element Simulations of Contact Heat Transfer on a Batch-Operated Single Floor of a Multiple Hearth Furnace," *Processes* 11 (2023): 3257, https://doi.org/10.3390/pr11123257.

16. J. Mačak, C. Goniva, and S. Radl, "Predictions of the P1 Approximation for Radiative Heat Transfer in Heterogeneous Granular Media," *Particuology* 82 (2023): 25–47, https://doi.org/10.1016/j.partic.2023.01.003.

17. M. De Beer, "Characterisation of Thermal Radiation in the Near-Wall Region of a Packed Pebble Bed" (master's thesis, North-West University, 2014).

18. E. Illana Mahiques, M. Brömmer, S. Wirtz, and V. Scherer, "Locally Resolved Simulation of Gas Mixing and Combustion Inside Static and Moving Particle Assemblies," *Chemical Engineering Technology* 46 (2023): 1362–1372, https://doi.org/10.1002/ceat.202200622.